

Simulation of soot particle morphology in a premixed ethylene stagnation flame

Dingyu Hou^{1,2}, Casper S. Lindberg^{3,4}, Mengda Wang^{1,2},
Manoel Y. Manuputty^{3,4}, Xiaoqing You^{1,2}, Markus Kraft^{3,4,5}

released: August 5, 2019

¹ Center for Combustion Energy
Tsinghua University
Beijing, 100084
China

² Key Laboratory for Thermal Science
and Power Engineering of
the Ministry of Education
Tsinghua University
Beijing, 100084
China

³ Department of Chemical Engineering
and Biotechnology
University of Cambridge
Philippa Fawcett Drive
Cambridge, CB3 0AS
United Kingdom

⁴ CARES
Cambridge Centre for Advanced
Research and Education in Singapore
1 Create Way
CREATE Tower, #05-05
Singapore, 138602

E-mail: mk306@cam.ac.uk

⁵ School of Chemical
and Biomedical Engineering
Nanyang Technological University
62 Nanyang Drive
Singapore, 637459

Preprint No. 233



Keywords: soot, aggregate morphology, population balance simulation, primary particle size distribution

Edited by

Computational Modelling Group
Department of Chemical Engineering and Biotechnology
University of Cambridge
Philippa Fawcett Drive
Cambridge CB3 0AS
United Kingdom

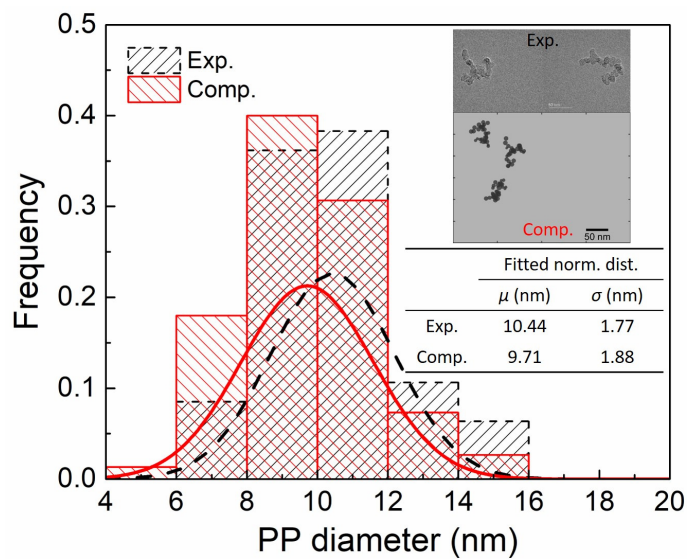
E-Mail: c4e@cam.ac.uk

World Wide Web: <http://como.ceb.cam.ac.uk/>



Abstract

Numerical simulation of soot formation in a laminar premixed burner-stabilized ethylene stagnation flame was performed with a detailed population balance model (DPBM) capable of tracking full structural details of aggregates as well as their chemical composition. A thorough parametric sensitivity study was carried out to understand the influence of individual sooting processes on the computed primary particle size distributions (PPSDs). The rate of production of pyrene, coagulation efficiency, surface growth rate and sintering/coalescence rate were found to have significant effects on the computed PPSDs, while sintering of aggregates only had mild effects. Direct comparison between the computed and observed aggregate morphology was performed both qualitatively and quantitatively. Excellent agreement was obtained, demonstrating the capability of the current DPBM in predicting aggregate morphology and supporting the current mechanisms contributing to the evolution of primary particles (PPs), i.e. nucleation, coagulation, surface growth and sintering/coalescence. The rates of individual sooting processes were examined to determine the dominant particle processes at different periods of time, which helped explain the time evolution of the PP size. Despite of the encouraging agreement between the computed and measured morphology of aggregate particles, we suggest that a more fundamental study of the coalescence process is required.



Highlights

- Morphology of soot aggregates in a premixed ethylene flame was computed using a detailed model and compared with experimental TEM images directly.
- A thorough parametric sensitivity study was performed to understand the influence of key model parameters on the predicted soot aggregate morphology.
- Time scale analysis for individual sooting processes were conducted to explain the morphological evolution of soot particles.

Contents

1	Introduction	3
2	Modelling methodology	5
2.1	Target flame	5
2.2	Flame model	5
2.3	Gas-phase chemistry model	5
2.4	Particle model	6
2.5	Numerical method	8
3	Results and discussion	9
3.1	Parametric sensitivity study	9
3.2	Comparison with experimental results	12
3.3	Time scale analysis for individual processes	14
4	Conclusions	18
	References	22

1 Introduction

Soot, as one of the particulate by-products of the incomplete combustion of hydrocarbon fuels, is a major air pollutant and a potential threat to human health [45, 57]. In contrast, carbon black (CB), a kind of carbonaceous particle sharing similar formation mechanisms with soot, is very versatile in industry, such as reinforcer in automobile tires and pigment in laser printers [13, 14, 57]. Knowledge regarding the mechanisms of soot formation will not only help mitigate pollutant emission during combustion, but also improve the production efficiency of CB in industry. For this purpose, much research has been conducted to explore soot formation mechanisms in the past several decades. Experimentally, a variety of characteristics of soot particles including the volume fraction [10, 52, 59], particle size [2, 36, 54], morphology [1, 49, 50], fine structure [6, 55], and molecular composition [12, 51] have been measured using different techniques. Meanwhile, a number of mechanisms for individual sooting processes, for instance the well-known Hydrogen-abstraction-C₂H₂-addition (HACA) mechanism for soot surface growth, were proposed [19]. In order to verify whether these hypothesized sub-mechanisms are responsible for soot formation and growth, comparison between the simulated and measured results is required. Therefore, a variety of population balance models for soot have been developed. Performing sensitivity analysis on the basic processes in a soot model and comparing the results with experimental observations give clues to which of the sub-models need to be refined.

In previous modelling work, it is common to compare the computed integral properties of soot particles, such as the volume fraction [3], or more detailed information — such as the particle size distributions (PSDs) [5, 33, 46] with experimental results, while not enough attention has been paid to the simulation of aggregate morphology. One possible reason for the lack of studies on modelling soot aggregate morphology may be the lack of statistical experimental data characterising the morphology, such as the primary particle (PP) number and size distribution [7]. In addition, the limitations of the existing soot models are also responsible for this problem — soot models have to be detailed enough to track morphological information, while only a minor number of soot models in literature are capable of capturing full structural information of aggregate particles [29]. However, modelling studies focusing on the morphology of soot aggregates are actually needed, especially in the CB industry, because it is the morphology of CB that determines its end-use and performance, while the current techniques used to control the aggregate morphology are still based on trial and error [27, 40].

Early efforts on modelling aggregate morphology of soot were made by a few researchers. Mitchell and Frenklach [37] simulated the morphological evolution of a single aggregate particle experiencing simultaneous surface growth and aggregation using a dynamic Monte Carlo method, also called the collector-particle technique. They attributed the spheroidal shape of particles to rapid surface growth and intense particle nucleation. A follow-up study by the same authors introduced a shape descriptor to quantify particle geometry and examined the transition between the coalescent and fully-developed fractal aggregation regimes [38]. To extend the analysis of the dynamics of a single aggregate to the ensemble-averaged simulations, Balthasar and Frenklach [4] incorporated the results obtained in [37, 38] into the method of moments to calculate soot formation in premixed

flames. Further development of the collector-particle technique [37, 38] was carried forward by Morgan et al. [39], who combined the particle model in [37, 38] with an efficient stochastic particle collision algorithm [5, 42, 43] to perform population balance simulations of soot particles in laminar premixed flames. The model of Morgan et al. [39] was capable of tracking full structural details of soot particles undergoing nucleation, coagulation and surface growth. These studies demonstrated that the morphology of aggregate particles was the result of the complex interplay between individual processes — nucleation, surface growth and coagulation [37–39].

Discrete element modelling (DEM) is also a useful tool to investigate the morphological evolution of aggregate particles undergoing several particle processes, such as coagulation [15, 22, 23], surface growth [28] and sintering [16, 21]. For instance, Kelesidis et al. [28] studied the dynamics of carbonaceous aerosols from nascent to mature fully-developed soot structures during simultaneous agglomeration and surface growth. Correlations among gyration diameter, mobility diameter, PP diameter and particle effective density accounting for the PP polydispersity and chemical bonding were obtained based on their DEM simulations.

Despite the knowledge gained on the morphological evolution of soot particles from prior modelling efforts, there are still open questions concerning the mechanisms of PP evolution due to the complex nature of soot formation in flames, where multiple processes are taking place simultaneously. Besides nucleation, surface growth and coagulation, which were considered in the above mentioned modelling work, other mechanisms such as sintering and coalescence, through which particles become more round without mass addition, may also play an important role in the growth of primary soot particles. For instance, recent experimental work provided evidence of the sintering of soot particles [40], although some researchers speculated that sintering was less likely to happen on carbonaceous nanoparticles [38]. Therefore, a model capable of incorporating as many hypothesized mechanisms as possible is helpful to figure out the significance of each mechanism on the evolution of particle morphology. Detailed population balance models (DPBMs) for soot, developed by Kraft and co-workers [9, 48, 60], provide such an effective tool. In general, a DPBM represents soot particles as aggregates composed of overlapping PPs, where each PP is composed of a number of polycyclic aromatic hydrocarbons (PAHs). Botero et al. [7] employed a DPBM for the first time to investigate the mechanisms that are important for the prediction of the primary particle size distribution (PPSD) in a C_2H_4 co-flow laminar diffusion flame. They found that the parameterization of sintering and particle rounding processes had significant effect on the simulated PPSDs. However, the DPBM in [7] did not track the relative position of PPs within aggregates, leaving the aggregate morphology unresolved during simulation. A free model parameter — the smoothing factor σ was introduced to account for particle rounding due to mass addition processes, i.e. surface growth and condensation.

Recently, the limitations of the prior DPBM in [7] were overcome by Lindberg et al. [32] and Hou et al. [24] by tracking the coordinates of all PPs, thus the aggregate morphology can be resolved during simulation. The improved detailed type space allowed more physical description of particle processes such as surface growth and sintering [24, 32] to be incorporated. The free model parameter σ used in the previous model [7, 9, 60] was eliminated. With this improved DPBM, Hou et al. [24] simulated soot formation in

a benchmark premixed ethylene stagnation flame [8] and reasonable agreement between the simulated and measured PSDs was obtained. The parametric sensitivity study in [24] showed that the computed mobility diameters of aggregate particles were not very sensitive to the sintering rate, while the size of PPs constituting the aggregate particles can be significantly affected. Since no morphological data was available from the experimental investigation [8], for example transmission electron microscopy (TEM) images, comparison between simulated and observed soot morphology could not be conducted.

Recent experimental work of Wang et al. [58] reported the measured PPSD of soot particles produced in laminar premixed ethylene flames, with conditions similar to the benchmark flame that was simulated in our previous work. It would be of interest to test the performance of this improved DPBM in predicting the morphology of soot particles in premixed flames by comparing with experimental results. Therefore, the **purpose of this work** is threefold: 1) simulate the morphological evolution of soot particles in a premixed ethylene flame employing the improved DPBM [24], which is capable of resolving both morphology and composition of aggregate particles; 2) make direct comparison between the simulated morphology and experimental TEM images and PPSDs; 3) investigate the influence of key particle processes on the simulated soot aggregate morphology through parametric sensitivity study, especially the role of coalescence/sintering in the evolution of soot aggregate morphology.

2 Modelling methodology

2.1 Target flame

In this study, we modelled the burner-stabilized premixed ethylene stagnation flame of Wang et al. [58] (Flame A3 in [58]; stagnation plate height $H_p = 1.2$ cm). The experimental details are introduced in [58]. Briefly, the unburned gas composition is 16% C_2H_4 , 24% O_2 and 60% AR (molar basis); the inlet cold gas velocity is 7 cm/s and the temperature was 298 K; the temperature at the stagnation plate is around 465 K.

2.2 Flame model

The axisymmetric stagnation flow in the flame is modelled using a pseudo one-dimensional approximation, which is described in detailed in [2, 34, 60].

2.3 Gas-phase chemistry model

The gas-phase chemistry is determined by the ABF mechanism [3], which contains 101 species and 543 reactions, with pyrene (A4) being the largest PAH.

2.4 Particle model

Two different particle models — a spherical model and a detailed model are used during different simulation steps serving different purposes, which will be discussed in Section 2.5.

The spherical model, used in the first-step simulation, describes all soot particles as spheres composed of C atoms only. Three types of particle processes — inception, coagulation and surface reactions are incorporated. Inception is modelled as two A4 molecules sticking after collisions. Coagulation is modelled as the collision and instantaneously coalescence of two particles. Surface reactions include the reactions of gaseous C_2H_2 , H, O_2 , OH and A4 with the surface of soot particles. A more detailed description on the spherical model can be found in [3, 53].

The detailed particle model, employed in the post-processing step, represents soot particles as aggregates composed of overlapping spherical PPs, where each PP consists of a number of PAHs. Since a comprehensive description of this detailed particle model has been presented in our previous work [24, 32], only a brief introduction on the most important aspects of the model will be given below. Figure 1 illustrates the type space of the detailed particle model, i.e. the mathematical representation of a particle. An aggregate

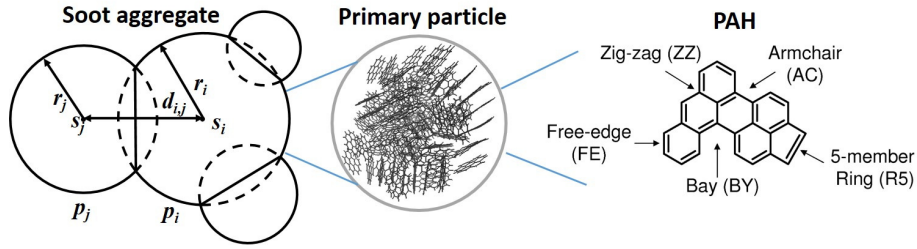


Figure 1: An illustration of the detailed particle model type space showing an aggregate particle (solid outlines) composed of PPs modelled as overlapping spheres (indicated by the dashed lines). PPs are composed of PAHs. The exact structure of PAHs are recorded. Redrawn based on [32, 44, 47]

particle, P_q , containing $n(P_q)$ overlapping PPs, is represented as

$$P_q = P_q(p_1, \dots, p_{n(P_q)}, \mathbf{D}), \quad (1)$$

where a PP p_i , with $i \in \{1, \dots, n(P_q)\}$ is represented as

$$p_i = p_i(m_1, \dots, m_{n(p_i)}, r_i, \mathbf{s}_i), \quad (2)$$

where m_x , with $x \in \{1, \dots, n(p_i)\}$, represents the exact structure of a planar PAH; $n(p_i)$ is the total number of PAHs within the primary p_i ; r_i is the radius of primary p_i ; \mathbf{s}_i represents the position of the center of the PP relative to the center of mass of the aggregate particle; \mathbf{D} is the connectivity matrix used to store the center to center separation $d_{i,j}$ of any two neighboring primaries p_i and p_j .

Six particle processes namely inception, coagulation, surface growth and oxidation, condensation, sintering and coalescence are incorporated in the detailed particle model, as

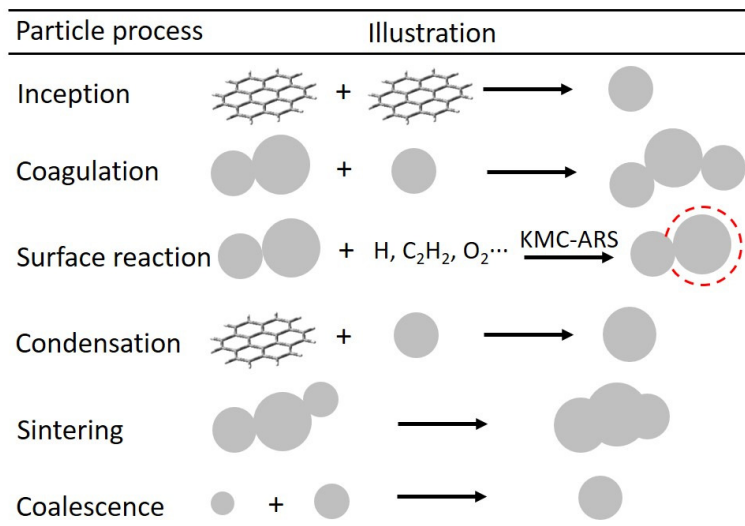


Figure 2: An illustration of particle processes incorporated in the detailed particle model.

illustrated in Fig. 2. A more detailed description of these particle processes can be found in our previous work [24, 32] and references therein.

Inception. Inception is modelled as two gaseous PAH molecules sticking together after collision. Two model parameters — inception mode (combined, minimum, maximum, reduced) and inception threshold are used to determine the sticking probability of two colliding PAHs. For example, the combined mode with inception threshold = 32 means two PAHs will stick together after collision if the sum of the number of aromatic rings in them exceeds 32, otherwise inception fails. Detailed discussion regarding the inception process and the influence of inception mode and threshold on the computed soot particle size distributions (PSDs) can be found in our previous work [24].

Coagulation. Coagulation is modelled as two particles (either primary or aggregate particle) sticking in point contact after collision. The rate of coagulation is calculated based on a transition regime coagulation kernel and a coagulation efficiency ($0 \leq \eta \leq 1$). The orientations of colliding particles and point of contact are determined by ballistic cluster-cluster aggregation (BCCA) with a random impact parameter [26]. A more detailed description can be found in [32].

Surface reaction. Surface growth and oxidation of a soot particle is modelled as the reactions of the PAHs inside the particle with gas-phase species, such as H and C₂H₂. The evolution of an individual PAH is described by the kinetic Monte-Carlo Aromatic Site (KMC-ARS) model [30, 44], where the reactions of PAH molecules are simplified to around 20 jump processes using the steady-state assumption. Two parameters — the critical number of PAHs inside a PP n_{crit} and the growth factor g are introduced to differentiate PAH growth in a large PP from growth in a small one. If the number of PAHs in a PP exceeds n_{crit} , a growth factor $g \in [0, 1]$ will be applied to the growth rate as a multiplier for all PAHs within that PP.

Condensation. Condensation is modelled as a gaseous PAH molecule sticking to a par-

ticle (either primary or aggregate particle) following a collision between them. A free model parameter — the condensation threshold is introduced to describe the sticking efficiency between a PAH and a particle. The sticking efficiency is 1 if the number of aromatic rings of the colliding PAH exceeds the condensation threshold, otherwise it is 0.

Sintering. Sintering refers to the process through which an aggregate particle becomes more round without gaining mass from gas-phase species. In the model, sintering is performed individually on each pair of neighboring primaries, p_i and p_j in an aggregate. During sintering, the centers of p_i and p_j approach and the diameters of p_i and p_j increase. A detailed mathematical description of sintering based on the aforementioned particle type space can be found elsewhere [17, 32]. The sintering rate R_{sint} is calculated by

$$R_{\text{sint}} = 1/\tau_s = 1/\left\{A_s d_{i,j} \exp\left[\frac{E_s}{T}\left(1 - \frac{d_{\text{crit}}}{d_{i,j}}\right)\right]\right\}, \quad (3)$$

where τ_s is the characteristic sintering time, with A_s (s/m) being the pre-exponential factor, $d_{i,j}$ (nm) being the minimum diameter of two neighboring PPs (i and j are indices of the two neighboring PPs), E_s (K) being the activation energy and d_{crit} (nm) being the critical PP diameter below which the primary particles are assumed to be liquid-like and will “coalesce” instantaneously [56].

Coalescence. Coalescence refers to the process by which two nascent spherical soot particles fuse into a larger spherical particle instantaneously after a collision. This infinitely fast restructuring process is due to the liquid-like nature of nascent soot particles. In fact, coalescence process can be regarded as a special situation of sintering process and it is actually described by the parameter d_{crit} in Eq. (3). Assume for instance a coagulation process is performed on two spherical particles, at least one of which has a diameter smaller than d_{crit} . Although coagulation of two particles leads to an aggregate particle with its two colliding partners in a point contact, Eq. (3) will produce an infinitely small τ_s i.e. an infinitely fast sintering rate for this aggregate particle if $d_{i,j} \leq d_{\text{crit}}$, thus this aggregate will immediately merge into a single spherical particle.

2.5 Numerical method

The numerical method consists of two steps. The purpose of the first-step simulation is to calculate the flame profile by coupling a gas-phase reaction model, a flow model and a spherical particle model. In this way, the effect of soot particle processes, i.e. inception and surface reactions on key gas-phase species can be approximately accounted for. Method of moments with interpolative closure (MoMIC) is employed to close the moment transport equations [18]. The *kinetics*[®] software package [11] is used to perform the first-step simulation.

In the second simulation step, the calculated gas-phase species profile is post-processed with a detailed particle model to resolve the morphology of soot particles. The particle population balance is solved by a stochastic method, with various enhancements to improve the efficiency [20, 41, 43]. This two-step modelling methodology is well established and has been applied in a number of previous works [7, 9, 60, 61]. Recently, Lindberg et al. [31] extended this methodology for stagnation flames. Detailed discussion regarding this methodology can be found in [31].

3 Results and discussion

Our previous work [24] focused on simulating the mobility diameter d_m of soot particles in premixed ethylene stagnation flames. However, two aggregate particles with different morphology, for instance, one aggregate particle composed of a large number of small PPs and the other composed of a small number of large PPs, can have similar d_m . Therefore, besides the mobility size of aggregate particles, the size of PPs will become the main issue of this work.

3.1 Parametric sensitivity study

A thorough parametric sensitivity study was carried out to understand the influence of key particle processes on the computed PPSDs. The initial values of key model parameters are based on our previous work [24], as listed in Table 1. When examining the influence of a certain parameter on the computed PPSD, the remaining parameters in the model were assigned their initial values.

Table 1: Key model parameters in the detailed soot model.

Parameter	Value
(1) Material property	
Soot density ρ (g/cm ³)	1.0
(2) Nucleation	
$\dot{\omega}_{A4}$ (mol/(cm ³ s))	Gas-phase input
Inception mode	Combined
Inception threshold ^a	32
(3) Condensation	
Condensation threshold ^a	4
(4) Surface growth	
Critical num. of PAH n_{crit}	1 (50) ^b
Growth factor g	1 (0.0263) ^b
(5) Coagulation	
Efficiency η	1 (Size & temperature dependent) ^b
(6) Sintering	
A_s (s/m)	1.10×10^{-14}
E_s (K)	9.61×10^4
d_{crit} (nm)	1.58 (3.0) ^b

^a The unit is number of aromatic rings.

^b Values (in parentheses) are applied when performing comparison between the computed and measured morphology of soot particles.

The influence of five model parameters including the rate of production of A4 $\dot{\omega}_{A4}$, coagulation efficiency η , surface growth factor g , pre-exponential factor A_s and critical diameter

of PP d_{crit} in the sintering sub-model on the computed PPSD will be introduced in the following section. Among these parameters, $\dot{\omega}_{A4}$ is related to the nucleation rate; η affects the coagulation rate; g controls the surface growth rate; A_s and d_{crit} determine the sintering/coalescence rate.

Figure 3(a) shows the effect of $\dot{\omega}_{A4}$ on the computed PPSDs. Although $\dot{\omega}_{A4}$ is not the same as the nucleation rate as one A4 molecule is not the equivalent of one just nucleated soot particle, A4 molecules are the starting point of the detailed population balance simulation, i.e. the post-processing step. To investigate the influence of $\dot{\omega}_{A4}$ on the simulated PPSDs, two different multipliers $\hat{\omega}_{A4}$ - 0.5 and 2.0 were applied to the original $\dot{\omega}_{A4}$ profile and served as the input to the post-processing step. As shown in Fig. 3(a), the computed PP diameter is larger when a larger $\dot{\omega}_{A4}$ profile is employed. This is because larger $\dot{\omega}_{A4}$ results in more PAHs and thus more small particles, which promotes coalescence and condensation and leads to larger PPs. In addition to the computed PPSDs, the effect of $\dot{\omega}_{A4}$ on the computed distribution of number of PP per aggregate was also investigated, as shown in Fig. 3(b). The computed aggregate particles tend to contain more PPs if a larger $\dot{\omega}_{A4}$ is used. This is because larger $\dot{\omega}_{A4}$ increases the number of particles by increasing number of freshly nucleated particles, thus promoting coagulation processes and resulting in aggregate particles containing more PPs.

Figure 3(c) shows the influence of coagulation efficiency η on the computed PPSDs. $\eta = 1$ leads to larger PPs than $\eta = 0.5$ or 0.1. Although coagulation does not seem to have any effect on the size of PPs, yet when particles are smaller than d_{crit} , after they coagulate with each other they will instantaneously merge into one single PP as the sintering rate dictated by Eq. (3) is infinitely fast under such condition. Therefore, PPs tend to be larger with a higher η as coalescence becomes more prevalent.

Surface growth of soot particles is modelled as the growth of their constituent PAHs, which is described by the KMC-ARS model [44]. In order to study the effect of surface growth rate on the computed PPSDs, different multipliers i.e. growth factor g were applied to the surface growth rate. Note that although the original purpose of model parameters g and n_{crit} are to consider the steric effects on particle surface growth, i.e. to differentiate the growth rate of a gas-phase PAH and that of a PAH inside a large PP composed of many PAHs, here we only focused on the effect of surface growth rate while the steric effects are neglected, as n_{crit} was always assigned 1 no matter what value of g was. As shown in Fig. 3(d), surface growth rate affects the shape of the computed PPSDs dramatically. A faster surface growth rate results in larger PPs and a broader PPSD.

As introduced in Section 2.4, both sintering and coalescence, which can be regarded as a special situation of sintering, will result in more round particles without gaining mass from gas-phase species. The sintering sub-model presented by Eq. (3) has the advantage of combining these two processes together by introducing the parameter d_{crit} . Eq. (3) was first proposed by Tsantilis et al. [56] to model the sintering process of silica particles. Chen et al. [9] incorporated this sintering sub-model to the detailed population balance model (DPBM) of soot and computed PSDs of soot in premixed ethylene flames. A model parameter data set with parameters of the sintering sub-model, i.e. d_{crit} and E_s included was obtained by a two-step parameter estimation against the median and coefficient of variation of experimental PSDs for various flames. Although reasonable agreement between the computed and measured PSDs was achieved with the optimized

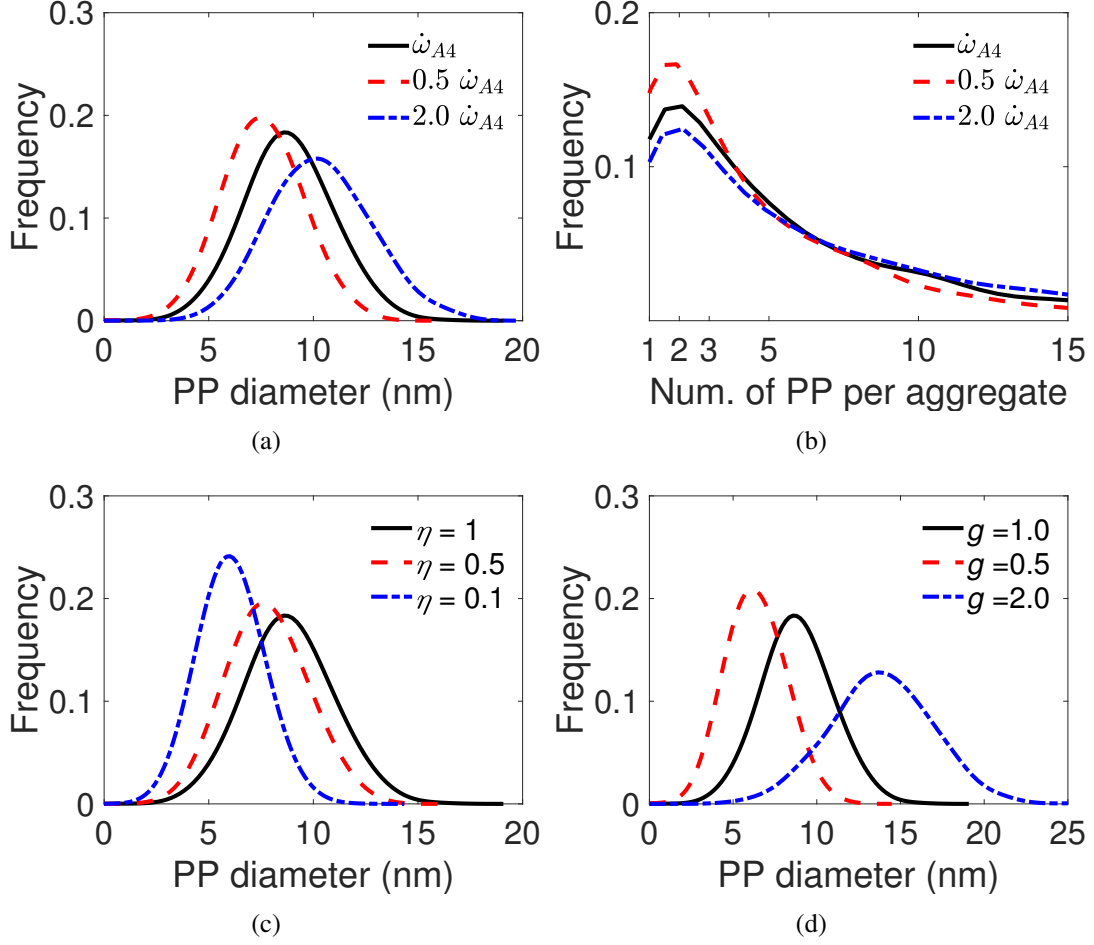


Figure 3: (a) The computed PPSDs with different rate of production of A4 ($\dot{\omega}_{A4}$); (b) The computed distribution of number of PPs per aggregate with different $\dot{\omega}_{A4}$; (c) The computed PPSDs with different collision efficiency; (d) The computed PPSDs with different surface growth rate.

model parameter data set in [9] (which is also listed in Table 1), large uncertainties of the parameters of the sintering sub-model could still exist. This is because d_{crit} had only limited effect on the computed PSDs while other parameters such as the rate of production of the precursor PAH molecules in the gas-phase and the collision efficiency of particles have more profound influence on the computed PSDs, as demonstrated in our previous work [24].

Fig. 4(a) shows the influence of the prefactor A_s in the sintering sub-model on the computed PPSD. The initial value of A_s is 10^{-14} s/m. Two more cases are shown with A_s increased or decreased by two orders of magnitude. Since $d_{\text{crit}} = 1.58$ nm remains unchanged when changing the value of A_s , the coalescence process of nascent soot particles, dictated by d_{crit} , is not affected. Therefore, changing the sintering rate by changing A_s mainly affects the sintering rate of soot aggregates. As demonstrated by Fig. 4(a), PPs are larger when $A_s = 10^{-16}$ s/m and smaller when $A_s = 10^{-12}$ s/m, which is understandable because a smaller A_s leads to a faster sintering rate and thus larger PPs.

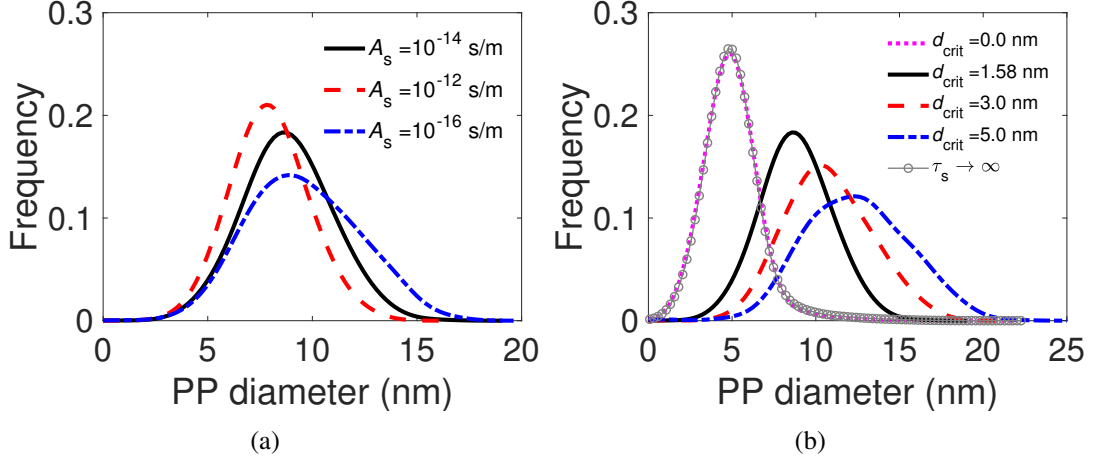


Figure 4: The computed PPSDs with different sintering rates. The sintering rate is changed by changing (a) A_s ; and (b) d_{crit} in Eq. (3), respectively.

Besides A_s , the sintering rate is also strongly associated with d_{crit} , which is in the exponential term in Eq. (3). The initial value of d_{crit} is 1.58 nm, indicating that when the diameter of a PP is smaller than 1.58 nm, it is liquid-like and will coalesce with its neighbor immediately. A larger d_{crit} leads to more coalescence processes, thus PPs are larger with $d_{\text{crit}} = 3.0\text{nm}$ and even larger with $d_{\text{crit}} = 5.0\text{nm}$. The extreme case with $d_{\text{crit}} = 0.0\text{nm}$ is also examined, in which there is no coalescence. It is noteworthy that $d_{\text{crit}} = 0.0\text{nm}$ does not mean the sintering rate is zero, instead the characteristic sintering time becomes

$$\tau_s = A_s d_{i,j} \exp \left[\frac{E_s}{T} \right]. \quad (4)$$

Although two colliding nascent soot particles cannot fuse into one larger particle immediately, they will still sinter at the rate dictated by Eq. (4) and eventually merge into a single spherical particle if the residence time for them is long enough. However, we find that the computed PPSD with no coalescence (represented by the magenta dotted line) almost coincides with that when the sintering sub-model is turned off, i.e. $\tau_s = \infty$ (represented by the solid gray line with open circles). This indicates the sintering of soot aggregates is rather slow and hardly affects the aggregate morphology. Fig. 4(a) and (b) together suggest that the sintering of soot aggregates only has a mild effect on the computed PPSD, while the coalescence of nascent soot particles, which is determined by d_{crit} , plays a critical role in the computed aggregate morphology. However, as mentioned earlier, large uncertainties can exist in d_{crit} . Given its significant influence on the predicted size of PPs, further study regarding the coalescence of soot particles, especially that from a fundamental point of view, is imperative in order to provide more instructive guidance on modelling the morphology of soot particles.

3.2 Comparison with experimental results

In succession to our previous work, in which the ability of the model to predict the PSD of soot formed in premixed ethylene flames was investigated [24], the performance of

the model in predicting the morphology of soot aggregates will be tested in this work by comparing the computed TEM-style images of soot particles with the experimentally observed ones.

Numerical simulation of soot formation in Flame A3 in [58] with $H_p = 1.2$ cm was carried out with the values of key model parameters listed in Table 1. The size and temperature dependent coagulation efficiency model of soot particles is based on our recent work [25]. Before comparing the computed and observed morphology of soot particles, the calculated and measured volume fraction (F_v) and PSD were compared first, as shown in Fig. 5. The deviation of the computed F_v (7.1×10^{-9}) from the measured value (2.5×10^{-8}) is around a factor of 3. Such agreement between the calculated and observed F_v is acceptable since the uncertainty of experimental data can also reach a factor of 3, as demonstrated in [8]. Besides F_v , reasonable agreement between the computed and measured PSD was also obtained.

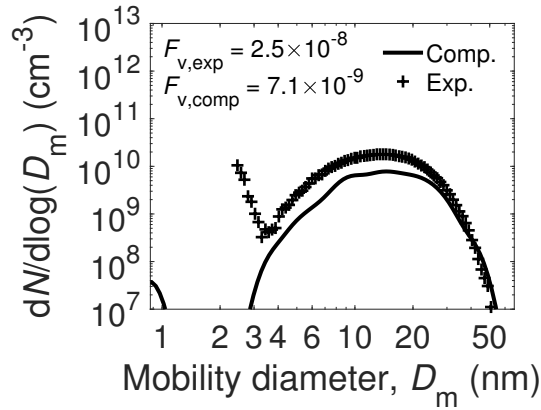


Figure 5: Comparison of the computed and measured PSD. The computed and measured volume fraction F_v were also noted. (Flame A3 in [58] with $H_p = 1.2$ cm)

As the calculated F_v and PSD are consistent with experimental measurements, further comparison between the calculated and observed morphology of soot aggregates was made, as illustrated by Fig. 6. The embedded pictures in Fig. 6 are the experimentally observed TEM image of soot particles with $d_m \approx 50$ nm taken from Wang et al. [58] and the computed TEM-style images of soot particles with $d_m \approx 50$ nm in this work, which appear quite similar. More quantitative comparison regarding the aggregate morphology was made by examining the calculated PPSD in this work and the experimental results in [58]. The experimental PPSD for particles with $d_m \approx 50$ nm, as shown in the black histogram in Fig. 6, was obtained by processing the observed TEM images and measuring the size of PPs using the software Image-Pro Plus [35]. For comparison, we have analyzed the size of all PPs within aggregates of d_m in the range of 40 – 50 nm based on our computational results and plotted the PPSD, as shown in the red histogram in Fig. 6. Normal distributions were fitted to the computed and measured PPSD, shown by the red solid line and black dashed line, respectively. The parameters of the fitted normal distributions, the median diameter μ and standard deviation σ , are given beside the PPSDs. Figure 6 demonstrates excellent agreement between the computed and the measured PPSD — not only are both of them unimodal in shape, but they also have similar median diameter (≈ 10 nm) and standard deviation (≈ 2 nm), which supports the current hypothesized

mechanisms contributing to the evolution of PPs — nucleation, surface growth, coalescence and sintering.

It is also pertinent to mention a recent study of Botero et al. [7], who investigated the evolution of PPs along the centreline of a co-flow laminar diffusion flame both experimentally and numerically. According to their experimental results [7], PPSDs at all heights-above-burner (HAB) were unimodal with a narrow width. However, the computed PPSDs appeared to be multi-modal rather than unimodal. The disagreement between the computed and measured PPSDs in [7] might be caused by the limitations of the DPBM that was employed, which did not track the coordinates of PPs within an aggregate, leaving the morphology of aggregates undetermined during the simulation. Moreover, due to the unresolved aggregate morphology, a free model parameter — smoothing factor σ was introduced to account for particle rounding due to mass growth processes. In contrast, the DPBM used in the current work eliminates the above mentioned limitations of the previous model by tracking aggregate morphology during simulation. The improvement of the DPBM may be part of the reason for the good agreement between the computed and measured PPSD in the current work. However, to examine whether the computed multi-modal PPSDs in [7] are due to the imperfection of the previous DPBM or some other factors, soot formation in the laminar diffusion ethylene flame in [7] needs to be investigated with the current DPBM. This will be investigated in a future study.

Despite the encouraging agreement, it is worth emphasizing that several model parameters may have large uncertainties due to the lack of understanding of individual sooting processes at the current stage. For example, d_{crit} in the sintering model, which is related to the coalescence of nascent soot particles, is assigned to be 3 nm in the current work. Although excellent agreement between the computed and measured PPSD is obtained with $d_{\text{crit}} = 3$ nm, more fundamental investigation such as molecular dynamics studies on the coalescence of soot particles are desired to provide evidence for the evaluation of d_{crit} .

Wang et al. [58] only examined the PPSD of soot particles with $d_m \approx 50$ nm, while the PPSDs of soot particles of other mobility diameters were not investigated experimentally. Hence, we studied whether the PPSD was sensitive to the size, i.e. d_m of aggregates from the modelling point of view. Normal distributions fitted to the computed PPSDs for soot particles with different d_m , 20, 30 and 40 nm are plotted in Fig. 7. The corresponding fitted parameters, σ and μ are also listed. The computed PPSDs in Fig. 7 almost coincide with each other, regardless of the d_m of aggregates. Fig. 7 together with Fig. 6 where the computed PPSD for particles with $d_m \approx 50$ nm is displayed, clearly demonstrate that PPSDs are insensitive to the size of aggregates. This suggests that the PPSD may become unchanged after a certain period of time. An in-depth discussion of this point will be given in subsequent sections.

3.3 Time scale analysis for individual processes

Soot formation is rather complicated as multiple particle processes may be happening at the same time. To determine the dominant particle processes at different stages of particle evolution, we examined the rate of individual sooting processes and plotted the results in Fig. 8. The rate of production of A4 ($\dot{\omega}_{A4}$), represented by the red solid line,

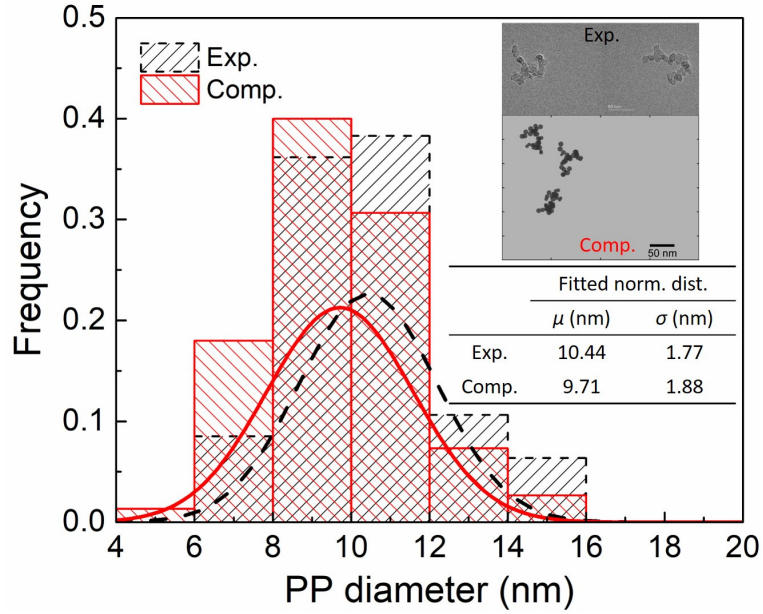


Figure 6: Comparison of the computed and experimental measured PPSDs. Lines are the fitted normal distributions. A representative experimental TEM image [58] and a computed TEM-style image of soot particles with $d_m \approx 50$ nm are embedded. (Flame A3 in [58] with $H_p = 1.2$ cm)

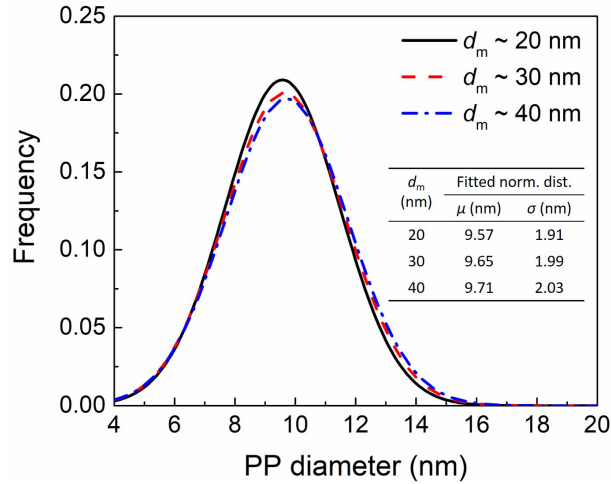


Figure 7: The computed PPSDs (fitted normal distributions) of soot particles with different d_m . (Flame A3 in [58] with $H_p = 1.2$ cm)

is calculated from the first-step simulation reflecting the inception intensity. The collision rate represented by the blue dashed line is actually the sum of the majorant kernels of all collision processes, namely inception (collisions between PAH molecules), condensation (collisions between PAH molecules and particles) and coagulation (collisions between particles). The majorant kernel is close to but larger than the real coagulation kernel, which is an algorithm used to speed up the stochastic simulations by reducing the complexity associated with solving the coagulation process [53]. The sintering rate, rep-

represented by the dash-dotted line, is calculated based on Eq. (3), where $d_{i,j}$ is estimated by the average diameter of all PPs. The curve of sintering rate is quite steep — before 30 ms, it is several orders of magnitude higher than other processes, while after 30 ms, it nearly stops. This is because the sintering rate is very sensitive to the PP diameter, as $d_{\text{crit}}/d_{i,j}$ is in the exponential term of Eq. (3). The mole fraction of H atoms is also plotted in Fig. 8 to indicate the rate of surface growth. According to the H-abstraction- C_2H_2 -addition (HACA) mechanism for soot surface growth, H atoms are required to provide growth sites for C_2H_2 molecules through H abstraction reactions [19]. Therefore, surface growth rate will be extremely low when the mole fraction of H drops to 10^{-6} . Hence, after 30 ms, coagulation becomes the only dominant process. Before 30 ms, the sintering rate can be several orders of magnitude larger than the rate of coagulation, hence aggregate structure can hardly appear at an early time stage.

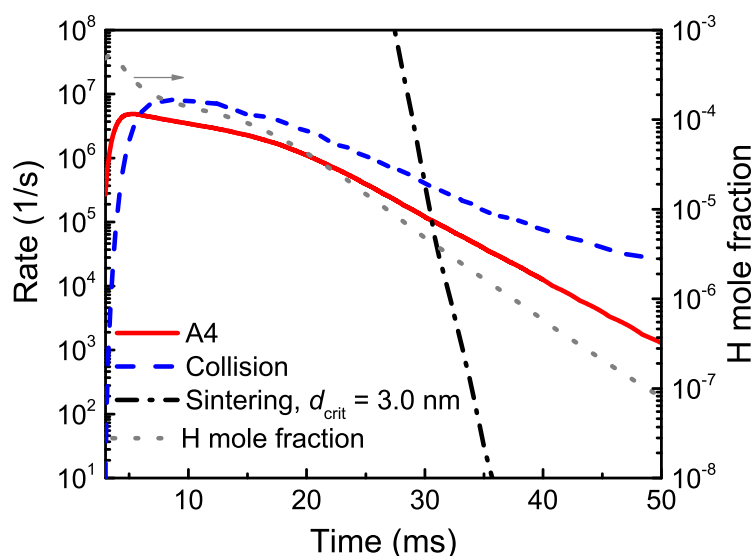


Figure 8: The rate of production of A4, collision rate and sintering rate (left Y-axis) and mole fraction of H (right Y-axis) against time.

With the knowledge gained from time scale analysis for individual particle processes, the evolution of average PP diameter and the average number of PP per aggregate with time were investigated, as illustrated in Fig. 9. Based on the slope of average d_{PP} against time, the growth of PP can be divided into three stages, as shown by the vertical dashed lines in Fig. 9. The first stage is from the beginning to 30 ms, where the growth of PPs is mainly due to surface growth and coalescence. Soot particles appear to be spherical at this stage, as the average number of PP per aggregate is 1, which is consistent with the time scale analysis for sintering process in Fig. 8. The second time stage spans from 30 to 50 ms, where the growth rate of PPs gradually slows down, as the slope of the average PP diameter against time is decreasing. This slow growth rate is also in consistent with Fig. 8, which demonstrates that both sintering and surface growth rate are rather slow during this time period. According to Fig. 8, the sintering rate declines drastically after 30 ms. In addition, the mole fraction of H atoms drops to near or below 10^{-6} , which is too low to provide enough reactive sites for surface growth. The last time stage is from 50 ms to the end of simulation, where the average PP diameter almost remains unchanged with

time, indicating both surface growth and sintering nearly cease. At this stage, coagulation becomes the leading process. The average number of PPs per aggregate increases linearly with time. Since both surface growth and coalescence contribute to the growth of PPs, we investigated the evolution of average d_{PP} without coalescence (i.e. $d_{crit} = 0$) to give an indication of the respective contribution of these two processes to the growth of PPs. This result is represented by the blue dash-dotted line in Fig. 9. With coalescence turned off, surface growth becomes the major contributor to the growth of PPs. In this situation, d_{PP} ends up at around 5 nm. By contrast, if coalescence process is incorporated, the final size of PPs can reach around 10 nm, much larger than the case when coalescence is turned off and agrees better with experimental observations.

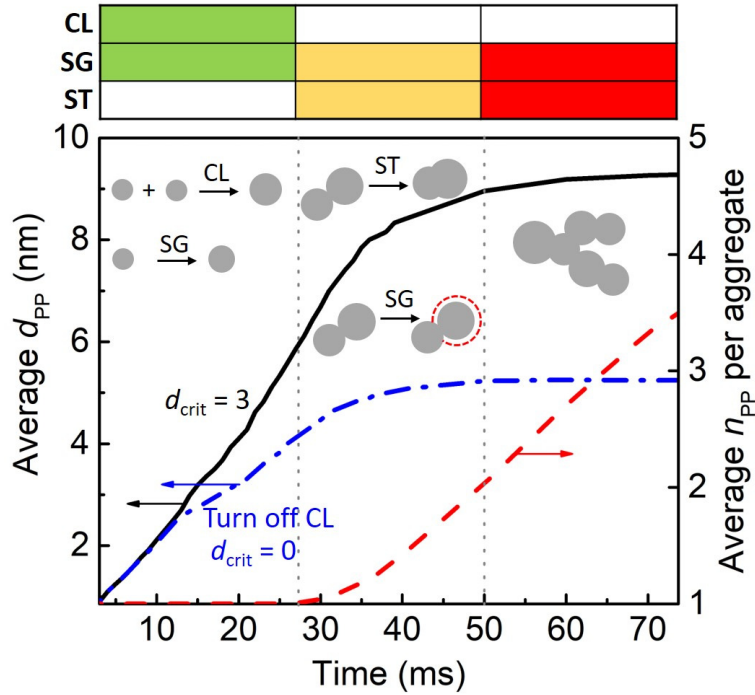


Figure 9: The computed time evolution of average PP diameter (left Y-axis) and average number of PPs per aggregate (right Y-axis). The table above suggests the rate of particle processes (CL: coalescence; SG: surface growth; ST: sintering) by different colors (Green: fast; Yellow: slow; Red: almost stop) at three time periods.

In addition to the time evolution of average d_{PP} , more detailed information — time evolution of the computed PPSD is illustrated in Fig. 10. The simulated PPSDs at five different times: 10, 20, 30, 50, 73.7 ms are shown. 73.7 ms corresponds to the residence time of a Lagrangian particle travelling from the burner to the stagnation plate at 1.2 cm. The conversion from distance to residence time is performed using the combined axial convective velocity and thermophoretic velocity, as described in our previous work [24, 31]. As shown by Fig. 10, the computed PPSDs evolve from a bimodal distribution (PPSDs at 10, 20 and 30 ms) to a unimodal distribution (PPSDs at 50 and 73.7 ms). We attribute the first peak of the bimodal PPSDs at earlier time stages to A4 molecules entering the simulation ensemble, because the d_{PP} corresponding to the first peak are always around

0.87 nm, which is the diameter of A4 molecules in the model. The peak with d_{pp} slightly larger than 0.87 nm can be caused by the growth of A4 to larger PAHs. In contrast, the second peak of the simulated PPSD can be attributed to the collision related processes, including the collisions between PAHs, PAH and particles or particles, all of which will lead to larger PPs. From 10 ms to 30 ms, the position of the second peak of the simulated PPSDs moves towards a larger diameter, which is caused by the persistent surface growth and coalescence in this period of time. Meanwhile, the intensity of the first peak is decreasing from 10 ms to 30 ms due to the decrease in $\dot{\omega}_{A4}$, as suggested by Fig. 8. At 50 ms, the first peak of the simulated PPSD corresponding to $\dot{\omega}_{A4}$ disappears, leaving a unimodal PPSD. After 50 ms, the modelled PPSD remains practically unaltered, as the computed PPSD at 73.7 ms coincides very well with that at 50 ms in Fig. 10. This is understandable because the size of PPs will change either by surface growth or coalescence/sintering, however, both processes nearly stop after 50 ms, leading to the simulated PPSD remaining unchanged.

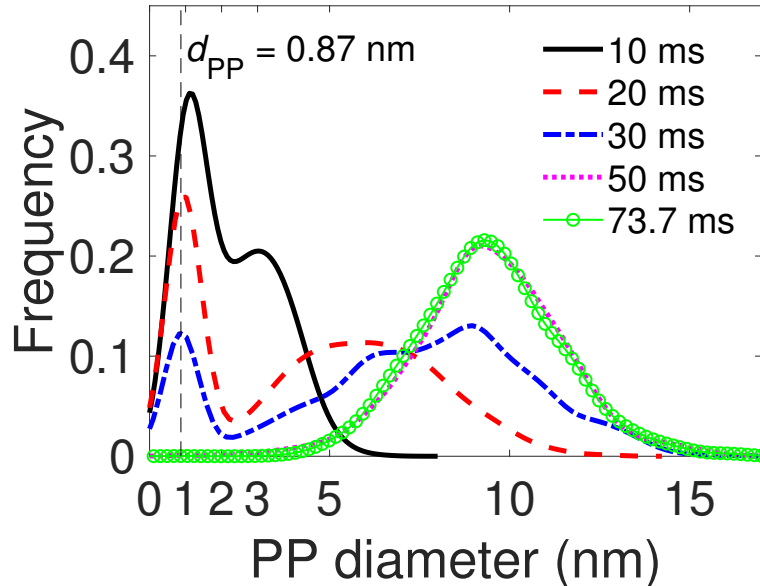


Figure 10: Time evolution of the computed PPSD. (Flame A3 in [58] with $H_p = 1.2$ cm)

4 Conclusions

In this work, we simulated soot formation in a premixed ethylene stagnation flame with a DPBM capable of tracking aggregate morphology as well as the chemical composition of soot particles. A thorough parametric sensitivity study was carried out to understand the influence of key particle processes on the computed PPSDs. The computed PPSDs were found to be sensitive to the rate of production of A4, coagulation rate and surface growth rate, which are in accordance with previous work. Besides, we found that coalescence played an important role in the computed aggregate morphology while sintering of soot aggregates only had mild influence on the predicted aggregate morphology.

Direct comparison between the computed and observed TEM images of soot particles was

performed both qualitatively and quantitatively. Excellent agreement between the computed and measured aggregate morphology was obtained, which demonstrated the ability of this DPBM to predict soot morphology and also supports the current mechanisms contributing to the evolution of soot PPs, i.e. nucleation, surface growth, coalescence and sintering.

Time scale analysis of individual particle processes was performed to determine the dominant processes at different time stages. Combining the results of time scale analysis for individual sooting processes and the time evolution of the average PP size and the number of PP per aggregate, the growth of PP can be divided into three different stages: the first of which has fast surface growth and coalescence; the second of which has slow surface growth and sintering; while surface growth and sintering almost stop in the third stage. The investigation of the time evolution of the computed PPSD demonstrates that the PPSD evolves from bi-modal to unimodal, which can be well explained by the interplay between nucleation, coalescence and surface growth. In addition, the computed PPSDs of soot particles in the premixed ethylene flame were shown to be insensitive to the size of aggregate particles.

However, despite of the encouraging agreement achieved between the computed and observed aggregate morphology, we suggest that more fundamental work regarding key individual particle processes is imperative. For instance, in this work $d_{\text{crit}} = 3 \text{ nm}$ was fitted and a more fundamental study (like molecular dynamics study) is needed to understand whether the value is appropriate. It is worth emphasizing that the current DPBM provides us with a powerful tool to investigate the key sooting processes by facilitating more direct comparison between computational results and experimental measurements. Further progress on soot modelling study can be made by reducing the uncertainties of key model parameters.

Acknowledgements

This project is supported by the National Research Foundation (NRF), Prime Minister's Office, Singapore under its Campus for Research Excellence and Technological Enterprise (CREATE) programme and the National Science Foundation of China (51761125012). The China Scholarship Council (CSC) is gratefully acknowledged. MK also acknowledges the support of the Alexander von Humboldt Foundation.

Nomenclature

Upper-case Roman

- A_s Pre-exponential factor, see Eq. (3)
- D_m Mobility diameter
- \mathbf{D} Connectivity matrix, see Eq. (1)
- E_s Activation energy, see Eq. (3)

F_v	Volume fraction
H_p	Stagnation plate height
P_q	Particle with index q , see Eq. (1)
R_{sint}	Sintering rate
T	Temperature

Lower-case Roman

d_{crit}	Critical primary particle diameter, see Eq. (3)
$d_{i,j}$	The minimum diameter of two neighboring primary particles, see Eq. (3)
d_m	Mobility diameter
d_{PP}	Diameter of primary particle
g	Growth factor
m_x	PAH with index x , see Eq. (2)
n_{crit}	Critical number of PAHs within a primary particle
$n(p_i)$	Number of PAHs in primary particle p_i , see Eq. (2)
$n(P_q)$	Number of primary particles in particle P_q , see Eq. (1)
p_i	Primary particle with index i
p_j	Primary particle with index j
r_i	Radius of primary particle p_i
\mathbf{s}_i	Position vector of the center of primary particle p_i to the center of mass of the aggregate, see Eq. (2)

Lower-case Greek

η	Coagulation efficiency
μ	Median diameter of normal distribution
ρ	Soot density
σ	Smoothing factor
σ	Standard deviation of normal distribution
τ_s	Characteristic sintering time
$\dot{\omega}_{\text{A4}}$	Rate of production of A4

Symbols

A4	Pyrene
----	--------

Abbreviations

ABF	Appel, Bockhorn, Frenklach
CB	Carbon black
DEM	Discrete element modelling
DPBM	Detailed population balance model
HACA	Hydrogen-abstraction-C ₂ H ₂ -addition

KMC-ARS	Kinetic Monte-Carlo - Aromatic site
MOMIC	Method of moments with interpolative closure
PAH	Polycyclic aromatic hydrocarbon
PP	Primary particle
PSD	Particle size distribution
PPSD	Primary particle size distribution
TEM	Transmission electron microscopy

References

- [1] A. D. Abid, N. Heinz, E. D. Tolmachoff, D. J. Phares, C. S. Campbell, and H. Wang. On evolution of particle size distribution functions of incipient soot in premixed ethylene-oxygen-argon flames. *Combustion and Flame*, 154:775 – 788, 2008. doi:10.1016/j.combustflame.2008.06.009.
- [2] A. D. Abid, J. Camacho, D. A. Sheen, and H. Wang. Quantitative measurement of soot particle size distribution in premixed flames – the burner-stabilized stagnation flame approach. *Combustion and Flame*, 156:1862 – 1870, 2009. doi:10.1016/j.combustflame.2009.05.010.
- [3] J. Appel, H. Bockhorn, and M. Frenklach. Kinetic modeling of soot formation with detailed chemistry and physics: laminar premixed flames of C2 hydrocarbons. *Combustion and Flame*, 121:122 – 136, 2000. doi:10.1016/S0010-2180(99)00135-2.
- [4] M. Balthasar and M. Frenklach. Detailed kinetic modeling of soot aggregate formation in laminar premixed flames. *Combustion and Flame*, 140:130 – 145, 2005. doi:10.1016/j.combustflame.2004.11.004.
- [5] M. Balthasar and M. Kraft. A stochastic approach to calculate the particle size distribution function of soot particles in laminar premixed flames. *Combustion and Flame*, 133:289 – 298, 2003. doi:10.1016/S0010-2180(03)00003-8.
- [6] M. L. Botero, D. Chen, S. González-Calera, D. Jefferson, and M. Kraft. HRTEM evaluation of soot particles produced by the non-premixed combustion of liquid fuels. *Carbon*, 96:459 – 473, 2016. doi:10.1016/j.carbon.2015.09.077.
- [7] M. L. Botero, N. Eaves, J. A. Dreyer, Y. Sheng, J. Akroyd, W. Yang, and M. Kraft. Experimental and numerical study of the evolution of soot primary particles in a diffusion flame. *Proceedings of the Combustion Institute*, 2018. doi:10.1016/j.proci.2018.06.185.
- [8] J. Camacho, C. Liu, C. Gu, H. Lin, Z. Huang, Q. Tang, X. You, C. Saggese, Y. Li, H. Jung, L. Deng, I. Wlokas, and H. Wang. Mobility size and mass of nascent soot particles in a benchmark premixed ethylene flame. *Combustion and Flame*, 162:3810 – 3822, 2015. doi:10.1016/j.combustflame.2015.07.018.
- [9] D. Chen, Z. Zainuddin, E. K. Y. Yapp, J. Akroyd, S. Mosbach, and M. Kraft. A fully coupled simulation of PAH and soot growth with a population balance model. *Proceedings of the Combustion Institute*, 34:1827 – 1835, 2013. doi:10.1016/j.proci.2012.06.089.
- [10] M. Choi, G. Mulholland, A. Hamins, and T. Kashiwagi. Comparisons of the soot volume fraction using gravimetric and light extinction techniques. *Combustion and Flame*, 102:161 – 169, 1995. doi:10.1016/0010-2180(94)00282-W.
- [11] CMCL Innovations. kinetics[®], 2016.

- [12] M. Commodo, K. Kaiser, G. D. Falco, P. Minutolo, F. Schulz, A. D’Anna, and L. Gross. On the early stages of soot formation: Molecular structure elucidation by high-resolution atomic force microscopy. *Combustion and Flame*, 205:154 – 164, 2019. doi:10.1016/j.combustflame.2019.03.042.
- [13] A. D’Anna. Combustion-formed nanoparticles. *Proceedings of the Combustion Institute*, 32:593 – 613, 2009. doi:10.1016/j.proci.2008.09.005.
- [14] J.-B. Donnet. *Carbon black: science and technology*. CRC Press, 1993.
- [15] M. L. Eggersdorfer and S. E. Pratsinis. The structure of agglomerates consisting of polydisperse particles. *Aerosol Science and Technology*, 46:347–353, 2012. doi:10.1080/02786826.2011.631956.
- [16] M. L. Eggersdorfer and S. E. Pratsinis. Restructuring of aggregates and their primary particle size distribution during sintering. *AIChE Journal*, 59:1118–1126, 2013. doi:10.1002/aic.14043.
- [17] M. L. Eggersdorfer, D. Kadau, H. J. Herrmann, and S. E. Pratsinis. Multiparticle sintering dynamics: From fractal-like aggregates to compact structures. *Langmuir*, 27:6358–6367, 2011. doi:10.1021/la200546g.
- [18] M. Frenklach. Method of moments with interpolative closure. *Chemical Engineering Science*, 57:2229 – 2239, 2002. doi:10.1016/S0009-2509(02)00113-6.
- [19] M. Frenklach and H. Wang. Detailed modeling of soot particle nucleation and growth. *Symposium (International) on Combustion*, 23:1559 – 1566, 1991. doi:10.1016/S0082-0784(06)80426-1.
- [20] M. Goodson and M. Kraft. An efficient stochastic algorithm for simulating nanoparticle dynamics. *Journal of Computational Physics*, 183:210 – 232, 2002. doi:10.1006/jcph.2002.7192.
- [21] E. Goudeli, M. L. Eggersdorfer, and S. E. Pratsinis. Aggregate characteristics accounting for the evolving fractal-like structure during coagulation and sintering. *Journal of Aerosol Science*, 89:58 – 68, 2015. doi:10.1016/j.jaerosci.2015.06.008.
- [22] E. Goudeli, M. L. Eggersdorfer, and S. E. Pratsinis. Coagulation-agglomeration of fractal-like particles: Structure and self-preserving size distribution. *Langmuir*, 31:1320–1327, 2015. doi:10.1021/la504296z.
- [23] E. Goudeli, M. L. Eggersdorfer, and S. E. Pratsinis. Coagulation of agglomerates consisting of polydisperse primary particles. *Langmuir*, 32:9276–9285, 2016. doi:10.1021/acs.langmuir.6b02455.
- [24] D. Hou, C. S. Lindberg, M. Y. Manuputty, X. You, and M. Kraft. Modelling soot formation in a benchmark ethylene stagnation flame with a new detailed population balance model. *Combustion and Flame*, 203:56 – 71, 2019. doi:10.1016/j.combustflame.2019.01.035.

- [25] D. Hou, D. Zong, C. Lindberg, M. Kraft, and X. You. On the coagulation efficiency of carbonaceous nanoparticles. 2019. Manuscript in preparation.
- [26] R. Jullien. Transparency effects in cluster-cluster aggregation with linear trajectories. *Journal of Physics A: Mathematical and General*, 17:L771, 1984.
- [27] G. A. Kelesidis, E. Goudeli, and S. E. Pratsinis. Flame synthesis of functional nanostructured materials and devices: Surface growth and aggregation. *Proceedings of the Combustion Institute*, 36:29 – 50, 2017. doi:10.1016/j.proci.2016.08.078.
- [28] G. A. Kelesidis, E. Goudeli, and S. E. Pratsinis. Morphology and mobility diameter of carbonaceous aerosols during agglomeration and surface growth. *Carbon*, 121: 527 – 535, 2017. doi:10.1016/j.carbon.2017.06.004.
- [29] M. Kraft. Modelling of particulate processes. *KONA Powder and Particle Journal*, 23:18–35, 2005. doi:10.14356/kona.2005007.
- [30] G. Leon, N. Eaves, J. Akroyd, S. Mosbach, and M. Kraft. A new methodology to calculate process rates in a kinetic Monte Carlo model of PAH growth. *Combustion and Flame*, 209:133 – 143, 2019. doi:10.1016/j.combustflame.2019.07.032.
- [31] C. S. Lindberg, M. Y. Manuputty, J. Akroyd, and M. Kraft. A two-step simulation methodology for modelling stagnation flame synthesised aggregate nanoparticles. *Combustion and Flame*, 202:143 – 153, 2019. doi:10.1016/j.combustflame.2019.01.010.
- [32] C. S. Lindberg, M. Y. Manuputty, E. K. Yapp, J. Akroyd, R. Xu, and M. Kraft. A detailed particle model for polydisperse aggregate particles. *Journal of Computational Physics*, 2019. doi:10.1016/j.jcp.2019.06.074.
- [33] R. Lindstedt and B. Waldheim. Modeling of soot particle size distributions in premixed stagnation flow flames. *Proceedings of the Combustion Institute*, 34:1861 – 1868, 2013. doi:10.1016/j.proci.2012.05.047.
- [34] M. Y. Manuputty, J. Akroyd, S. Mosbach, and M. Kraft. Modelling TiO₂ formation in a stagnation flame using method of moments with interpolative closure. *Combustion and Flame*, 178:135 – 147, 2017. doi:10.1016/j.combustflame.2017.01.005.
- [35] Media Cybernetics, Inc. Image-Pro Plus 7, 2018.
- [36] J. Mei, M. Wang, D. Hou, Q. Tang, and X. You. Comparative study on nascent soot formation characteristics in laminar premixed acetylene, ethylene, and ethane flames. *Energy & Fuels*, 32:11683–11693, 2018. doi:10.1021/acs.energyfuels.8b02852.
- [37] P. Mitchell and M. Frenklach. Monte Carlo simulation of soot aggregation with simultaneous surface growth — why primary particles appear spherical. *Symposium (International) on Combustion*, 27:1507 – 1514, 1998. doi:10.1016/S0082-0784(98)80558-4.

- [38] P. Mitchell and M. Frenklach. Particle aggregation with simultaneous surface growth. *Phys. Rev. E*, 67:061407, Jun 2003. doi:10.1103/PhysRevE.67.061407.
- [39] N. Morgan, M. Kraft, M. Balthasar, D. Wong, M. Frenklach, and P. Mitchell. Numerical simulations of soot aggregation in premixed laminar flames. *Proceedings of the Combustion Institute*, 31:693 – 700, 2007. doi:10.1016/j.proci.2006.08.021.
- [40] K. Ono, K. Dewa, Y. Matsukawa, Y. Saito, Y. Matsushita, H. Aoki, K. Era, T. Aoki, and T. Yamaguchi. Experimental evidence for the sintering of primary soot particles. *Journal of Aerosol Science*, 105:1 – 9, 2017. doi:10.1016/j.jaerosci.2016.11.013.
- [41] R. Patterson, J. Singh, M. Balthasar, M. Kraft, and J. Norris. The linear process deferment algorithm: A new technique for solving population balance equations. *SIAM Journal on Scientific Computing*, 28:303–320, 2006. doi:10.1137/040618953.
- [42] R. I. Patterson and M. Kraft. Models for the aggregate structure of soot particles. *Combustion and Flame*, 151:160 – 172, 2007. doi:10.1016/j.combustflame.2007.04.012.
- [43] R. I. Patterson, J. Singh, M. Balthasar, M. Kraft, and W. Wagner. Extending stochastic soot simulation to higher pressures. *Combustion and Flame*, 145:638–642, 2006. doi:10.1016/j.combustflame.2006.02.005.
- [44] A. Raj, M. Celnik, R. Shirley, M. Sander, R. Patterson, R. West, and M. Kraft. A statistical approach to develop a detailed soot growth model using PAH characteristics. *Combustion and Flame*, 156:896 – 913, 2009. doi:10.1016/j.combustflame.2009.01.005.
- [45] H. Richter and J. Howard. Formation of polycyclic aromatic hydrocarbons and their growth to soot — A review of chemical reaction pathways. *Progress in Energy and Combustion Science*, 26:565 – 608, 2000. doi:10.1016/S0360-1285(00)00009-5.
- [46] C. Saggese, S. Ferrario, J. Camacho, A. Cuoci, A. Frassoldati, E. Ranzi, H. Wang, and T. Faravelli. Kinetic modeling of particle size distribution of soot in a premixed burner-stabilized stagnation ethylene flame. *Combustion and Flame*, 162:3356 – 3369, 2015. doi:10.1016/j.combustflame.2015.06.002.
- [47] M. Sander. *Mathematical modelling of nanoparticles from gas-phase*. PhD thesis, University of Cambridge, 2011.
- [48] M. Sander, R. I. Patterson, A. Braumann, A. Raj, and M. Kraft. Developing the PAH-PP soot particle model using process informatics and uncertainty propagation. *Proceedings of the Combustion Institute*, 33:675 – 683, 2011. doi:10.1016/j.proci.2010.06.156.
- [49] M. Schenk, S. Lieb, H. Vieker, A. Beyer, A. Gölzhäuser, H. Wang, and K. Kohse-Höinghaus. Imaging nanocarbon materials: Soot particles in flames are not structurally homogeneous. *ChemPhysChem*, 14:3248–3254, 2013. doi:10.1002/cphc.201300581.

- [50] M. Schenk, S. Lieb, H. Vieker, A. Beyer, A. Gölzhäuser, H. Wang, and K. Kohse-Höinghaus. Morphology of nascent soot in ethylene flames. *Proceedings of the Combustion Institute*, 35:1879 – 1886, 2015. doi:10.1016/j.proci.2014.05.009.
- [51] F. Schulz, M. Commodo, K. Kaiser, G. D. Falco, P. Minutolo, G. Meyer, A. D’Anna, and L. Gross. Insights into incipient soot formation by atomic force microscopy. *Proceedings of the Combustion Institute*, 37:885 – 892, 2019. doi:10.1016/j.proci.2018.06.100.
- [52] C. R. Shaddix and K. C. Smyth. Laser-induced incandescence measurements of soot production in steady and flickering methane, propane, and ethylene diffusion flames. *Combustion and Flame*, 107:418 – 452, 1996. doi:10.1016/S0010-2180(96)00107-1.
- [53] J. Singh. *Detailed soot modelling in laminar premixed flames*. PhD thesis, University of Cambridge, 2006.
- [54] Q. Tang, R. Cai, X. You, and J. Jiang. Nascent soot particle size distributions down to 1 nm from a laminar premixed burner-stabilized stagnation ethylene flame. *Proceedings of the Combustion Institute*, 36:993 – 1000, 2017. doi:10.1016/j.proci.2016.08.085.
- [55] P. D. Teini, D. M. Karwat, and A. Atreya. Observations of nascent soot: Molecular deposition and particle morphology. *Combustion and Flame*, 158:2045 – 2055, 2011. doi:10.1016/j.combustflame.2011.03.005.
- [56] S. Tsantilis, H. Briesen, and S. E. Pratsinis. Sintering time for silica particle growth. *Aerosol Science and Technology*, 34:237–246, 2001. doi:10.1080/02786820119149.
- [57] H. Wang. Formation of nascent soot and other condensed-phase materials in flames. *Proceedings of the Combustion Institute*, 33:41 – 67, 2011. doi:10.1016/j.proci.2010.09.009.
- [58] M. Wang, Q. Tang, J. Mei, and X. You. On the effective density of soot particles in premixed ethylene flames. *Combustion and Flame*, 198:428 – 435, 2018. doi:10.1016/j.combustflame.2018.10.004.
- [59] F. Xu, P. Sunderland, and G. Faeth. Soot formation in laminar premixed ethylene/air flames at atmospheric pressure. *Combustion and Flame*, 108:471 – 493, 1997. doi:10.1016/S0010-2180(96)00200-3.
- [60] E. K. Y. Yapp, D. Chen, J. Akroyd, S. Mosbach, M. Kraft, J. Camacho, and H. Wang. Numerical simulation and parametric sensitivity study of particle size distributions in a burner-stabilised stagnation flame. *Combustion and Flame*, 162:2569 – 2581, 2015. doi:10.1016/j.combustflame.2015.03.006.
- [61] E. K. Y. Yapp, R. I. Patterson, J. Akroyd, S. Mosbach, E. M. Adkins, J. H. Miller, and M. Kraft. Numerical simulation and parametric sensitivity study of optical band gap in a laminar co-flow ethylene diffusion flame. *Combustion and Flame*, 167:320 – 334, 2016. doi:10.1016/j.combustflame.2016.01.033.